Multi-scale material modelling to predict the material anisotropy of multi-phase steels

Sathish Kumar Ravi[a,*], Marc Seefeldt[b], Albert Van Bael[b], Jerzy Gawad[a], Dirk Roose[a]

[a] *KU Leuven, Department of Computer Science, Celestijnenlaan 200A, 3001 Leuven, Belgium*
[b] *KU Leuven, Department of Materials Engineering, Kasteelpark Arenberg 44 bus 2450, 3001 Leuven, Belgium*

Abstract

In this article, a novel material modelling approach to predict the anisotropic material response of multi-phase steels is developed. The macroscopic material behaviour of the model is characterized by the homogenized response of a meso-scale Representative Volume Element (RVE), derived by Finite Element (FE) simulations. The RVE holds the most relevant microstructural features of the material under consideration, such as phase distribution, grain orientation, morphology etc., in sufficient detail, in order to capture the anisotropy and phase interactions. The micro-scale material models of individual phases are described with specific plastic potential functions, the components of which are derived from Crystal Plasticity (CP) laws. The plastic potential functions are constructed using the Facet method for each phase in the microstructure at the level of single grains, and are used in conjuncture with phase specific, isotropic grain hardening laws. The proposed model is evaluated through numerical experiments performed on a synthetic microstructure of Duplex steel, constructed from statistical material parameters extracted from literature. The RVE flow curves depicted very good correspondence with the experimental data reported for the same grade of Duplex Stainless Steel. The anisotropy prediction was further assessed through comparison between virtual diffraction experiments

*Corresponding author
Email address: SathishKumar.Ravi@cs.kuleuven.be (Sathish Kumar Ravi)

performed on the statistical microstructure and the actual Neutron Diffraction (ND) experimental data of the reference material. It was found that that the model captured the overall trend of the diffraction curves for the individual phases with good accuracy, but obtaining an exact correspondence to the experimental values was not feasible with the performed simulations on statistical microstructures. Finally, an approach to predict the anisotropic yield locus of a multi-phase material is also presented.

Keywords: `Multi-scale modelling, Multi-phase materials, Duplex steel, Representative Volume Elements, Plastic potential functions, Single Crystal Plasticity, Anisotropy, Yield locus`

1. Introduction

The macroscopic material response of multi-phase steels is extensively characterized by the inherent microstructural features such as phase composition and distribution, grain orientation and morphology, crystal structure etc. To predict a realistic response of multi-phase materials at the macro-scale, an accurate characterization of the multi-phase microstructure and homogenization of the microstructural response, are essential. Multi-scale simulations have gained extensive popularity in the field of material modelling over the past few decades and new numerical techniques are constantly added to the existing set. A comprehensive overview of the modern day challenges in the field of multi-scale modelling is given in an article published by Geers et al. [1]. Multi-scale simulations have numerous advantages for a variety of applications, despite being numerically expensive. They help in understanding the relation between the observed macroscopic phenomena and the underlying microstructure for diverse applications. Several works in literature have highlighted the importance of such hierarchical simulations in realizing the continuum behavior of materials encompassing distinct microstructures [2, 3, 4, 5, 6]. The complexity of the defined microstructure, in terms of their morphological features and material laws, influence the computational efficiency of these multi-scale numerical mod-

els. In this paper, we have developed a multi-scale framework to predict the macroscopic material behaviour of multi-phase steels, implemented in a computationally efficient manner.

The microstructure in a multi-scale simulation is often described by a Representative Volume Element (RVE) at the meso/micro-scale, incorporating the features of interest, with an underlying material definition to characterize the stress-strain response. The RVE can be described either by a discrete set of crystals (texture) or a well-resolved FE mesh with a unique spatial distribution of the associated features. For the latter involving RVEs with a distinct FE mesh, a constant drive towards sophisticated morphological description of the microstructural features is existent and there are several means in literature to achieve the same [7, 8, 9]. Some approaches have been translated into open source softwares as well [10, 11]. Development of new strategies requiring less experimental time and resources for the procurement of sufficient microstructure characterization data is an active field of research [12]. Further complications arise in numerical simulations of 3-Dimensional ($3D$) RVEs, ranging from the effort essential for an accurate description of the microstructural features in a $3D$ domain to the additional computational overhead in FE calculations. However, such additional efforts required for $3D$ RVE based simulations are often justified by their ability to replicate experimental observations. Several research works aimed at studying damage in DP steels through a coupled experimental-numerical approach, via 2D simulations, often report quantitative differences in capturing sharp strain localization bands from the experiments [13, 14]. It was often concluded to be the result of inability of the 2D microstructure based numerical simulations to address the sub-surface deformation mechanisms. There are also attempts made in this direction to capture the 3D behavior from 2D RVE simulations with isotropic material laws [7, 15, 16]. Also, there have been numerous works on RVE based simulation techniques for multi-phase steels with isotropic phases of different hardness. A unified formulation [17] to predict the flow behavior of steel phases have been predominantly used as material laws for such multi-phase simulations [8, 7, 18]. However, an isotropic description of the

material response at the microscopic level, would eventually fail to accurately capture the resultant anisotropy from the crystallography and phase interactions. Alternatively, with regard to Crystal Plasticity Finite Element Method (CPFEM) for modelling material anisotropy, an exhaustive summary has been provided in a recent review paper by Roters et al.[19]. A comprehensive overview of the constitutive laws that define the elasto-plastic behaviour of crystalline matter and different homogenization approaches have been elaborated in that article. The utilization of full field FE homogenization instead of the common Full Constraints Taylor [20], Taylor based relaxation schemes or other reduced homogenization methods, is deemed essential for a multi-phase material. This is supported by several experimental observations that ascertain the necessity of modelling the complementary phase behavior in order to thoroughly understand the microstructural effects. Such simple homogenization schemes cannot include critical features such as the stress and strain distribution among soft and hard phases, shear induced deformation through interactions, development of shear bands (strain localization) etc., observed in a multi-phase microstructure. Despite the advantages, the usage of sophisticated meso-/micro-models with full field CPFEM based homogenization, for a macroscopic simulation of engineering scale, would demand immense computational power and is in practice not feasible.

In recent times, the development of multi-scale simulation frameworks capable of addressing the aformentioned issues have gained momentum. Gawad et al. [21] have developed a hierarchical model, which can account for texture evolution in sheet forming simulations of single phase materials, driven by a texture dependent micro-scale plastic potential function derived via homogenization schemes such as Full Constraints (FC) Taylor or Advanced LAMEL (ALAMEL) [22]. DAMASK [23], Düsseldorf Advanced Material Simulation Kit, is another recently developed multi-scale simulation framework which is capable of modular CP implementations of different constitutive laws, homogenization methods and solvers. Kalidindi [24] has put forward an ambitious effort to address the current challenges in multi-scale computations through a data science

driven approach as well. In a multi-scale setup, incorporation of well defined meso-scale FE simulations is computationally less efficient. Hence, such RVE simulations based on rate-independent [25, 26, 27] or rate-dependent [28, 29, 30] CPFEM formulations are relatively scarce [31, 32], and even less in the domain of multi-phase materials [33]. As the development of diverse strategies within the context of a multi-scale simulation is always intriguing and challenging, here, we have constructed an efficient multi-scale model capable of extracting the macroscopic behaviour from meso-scale FE simulations coupled with a CP driven micro-scale model.

As elaborated above, a numerical model having the potential to capture the microstructural phenomena that drive the macroscopic behavior (e.g. metal forming), in sufficient detail, is of great importance. Specifically, in the case of multi-phase steels, the need to understand the behavior of the inherent phase components is essential. Coupling such a sophisticated approach with a CPFEM based material model would further enhance the complexity of a multi-scale simulation. Hence, in the present article, we aim at addressing these issues through a powerful micro-meso-macro approach, composed of generic components capable of undergoing amendments to suit the application. The model derives the homogenized macroscopic response of a synthetic multi-phase meso-scale RVE. The RVE is constructed from actual material parameters and includes a well-defined spatial description of the underlying phases/grains, with attached orientations. The material definitions that characterize the individual yield locus and the phase response are given by micro-scale single crystal plastic potential functions derived via the Facet approach [34]. Similar analytical expressions to describe the yield locus for single crystals were also reported in some earlier works in literature [35, 36, 37]. A more recent work to derive the yield functions of single crystals through optimization schemes was attempted by Zamiri et al. [38] as well. The Facet method, originally developed for single phase polycrystalline materials, constructs a plastic potential function calibrated by statistical texture simulations using crystal plasticity models. It can easily be coupled with a macroscopic domain for multi-scale simulations. A similar approach is

adopted in the developed model to arrive at the plastic potential functions of single crystals, representing the individual grain behavior with known orientation and crystallographic slip systems, based on the fundamentals of Crystal Plasticity (CP). In a later section we describe the steps involved in the derivation of the single crystal Facet expressions, which serve as the micro-scale material models for FE simulations on the meso-scale RVE. The multi-scale model can be applied on microstructures with varying crystalline phases and morphology. As long as the effects of microstructural evolution are minor or negligible, the description of plastic anisotropy through the proposed model would help understand the macro-scale response of the multi-phase microstructure. Eventually, a method to construct the anisotropic yield sections of multi-phase materials from RVE simulations, via the current model, is also discussed. There are several earlier works in literature that aim at the construction of the yield locus of polycrystalline aggregates of single phase materials [39]. However, attempts to characterize the same from microstructural FE simulations of multi-phase materials are relatively scarce [23]. The framework demonstrated in this article can also offer an efficient solution in this direction. It provides a powerful tool to study and quantify the yield behaviour in terms of different microstructural components from full-field FE simulations on the RVE. The effects of different parameters such as grain morphology, phase fraction and distribution, initial texture etc. of a well defined multi-phase 3D microstructure on the yield locus sections can be analysed. Also, such a scheme can eventually be used to construct plastic potential functions of the multi-phase RVE, which can be directly coupled to a macro-scale simulation.

The modelling framework is demonstrated through multi-scale simulations on a statistical microstructure of Duplex steel, consisting of Austenitic (FCC) and Ferritic (BCC) phases. The synthetic RVE was constructed using the material characterization information extracted from literature [40]. Due to the unavailability of experimental data, the authors have utilized the experimental data available from literature [40] for assessment of the numerical model. Uniaxial tensile test simulations were performed on the microstructure and the

homogenized response of the RVE was compared to the experimental data reported for the same grade of Duplex Stainless Steel. The anisotropy predictions by the developed model were further assessed through the comparison of lattice strains obtained from virtual diffraction simulations performed on the RVE, with those obtained from in situ neutron diffraction [41] experiments from the reference literature [40]. There are a number of similar works in literature that have performed a comparative study of lattice strain predictions with different numerical models for a variety of applications [42, 43, 44, 45]. In our case, the predicted diffraction curves for the individual phases, for different diffraction planes, were correlated with the ND experimental data. Finally, a yield locus section of the synthetic microstructure was also constructed.

This paper is organized as follows. An overview of the proposed model followed by a detailed explanation of individual components is described in Section 2. Section 3 describes the synthetic material characteristics and the FE model parameters, along with an account of the numerical simulations performed on the RVE. The results from the simulations are discussed in Section 4 and the important features of the framework are presented as well. Finally, the conclusive remarks are summarized in Section 5.

2. Multi-scale multi-phase numerical model

The proposed multi-scale numerical model is capable of predicting the macro-scale material response, averaged from the FE simulations on a meso-scale RVE, encapsulating a micro-scale material model derived from CP based material definitions. The numerical implementation of the model was established through an assembly of three distinct components, each corresponding to the existent scales in the set up.

- Micro-scale: Phase specific plastic potential functions in the stress space, at the level of individual grains, are derived from the theory of single crystal plasticity. For a given stress state, the plastic strain rate tensor is readily obtained from such a plastic potential function.

- Meso-scale: The RVE is constructed from the microstructural input parameters (unambiguous for a given material), incorporating the morphological features, phase information and grain orientations. The FE simulations are performed using an Abaqus VUMAT capable of handling material anisotropy and multiple phases, with the material response at each integration point defined by the phase specific plastic potential function.

- Macro-scale: The homogenized response of the RVE, obtained through volume averaging of each grain and phase, is considered to characterize the behaviour at every material point (or the integration point) of any macroscopic simulation.

2.1. Micro-scale: Single crystal plasticity based Facet plastic potential functions

The micro scale anisotropic material behavior of the phases in the RVE is defined through plastic potential functions obtained via the Facet method [34] for the single crystals of rate insensitive materials. Always, in a given time step of an elasto-plastic simulation, the gradient of a plastic potential function defined in the stress space ($\phi(\boldsymbol{\sigma})$ with $\boldsymbol{\sigma}$ being the stress tensor) would return the incremental plastic strain tensor, as

$$\begin{aligned} d\boldsymbol{\varepsilon} &= d\boldsymbol{\varepsilon}^e + d\boldsymbol{\varepsilon}^p \\ d\boldsymbol{\varepsilon}^p &= d\lambda \frac{\partial \phi}{\partial \boldsymbol{\sigma}}, \end{aligned} \tag{1}$$

where the positive scalar value $d\lambda$ is a proportionality factor, with $d\boldsymbol{\varepsilon}^e$ and $d\boldsymbol{\varepsilon}^p$ representing the elastic and plastic strain increments of the total strain tensor $d\boldsymbol{\varepsilon}$, respectively. In the associated flow theory based on the normality rule, such a plastic potential function is essentially the yield function of the given material. The calibration of such functions can be performed through mechanical tests as well as through simulations on multilevel models. The readers are requested to refer to literature for further understanding of such methods [35, 46, 34, 47], as an in depth explanation is beyond the scope of the article.

For our work, the focus is on the utilization of the Facet method to derive the plastic potential function of single crystals. For single crystals that obey the Generalized Schmid law of crystallographic slip, it is possible to define a convex yield surface with an associated plastic strain rate confined to the normality rule [48]. Starting from the laws of single crystal plasticity, we construct plastic potential functions described with respect to the crystal reference system, and they would eventually characterize the response of individual grains in the RVE with attached orientations. The function will evaluate the onset of yielding and will return the corresponding plastic strain rate vectors at every time step of the FE simulation, for each integration point. The establishment of such grain level plastic potential for individual phases of the multi-phase material can facilitate computationally faster FE simulations as compared to direct full field CPFEM simulations.

According to an earlier work on plastic potentials [35], from a plastic potential function $\Psi(\boldsymbol{S})$ for a polycrystal in deviatoric stress ($\boldsymbol{S}$) space, the plastic strain rate can be obtained as

$$D_p = \frac{1}{k}\frac{\partial \Psi}{\partial S_p}. \tag{2}$$

Here the index p denotes the components in a 5D deviatoric vector space. The plastic potential is described by a homogeneous expression of rank k as

$$\Psi(\eta \boldsymbol{S}) = \eta^k \Psi(\boldsymbol{S}) \quad \text{with} \quad \eta > 0 \quad \text{and hence} \quad D_p(\eta \boldsymbol{S}) = \eta^{k-1} D_p(\boldsymbol{S}). \tag{3}$$

Equation 3 can be satisfied by choosing the plastic potential to be a homogeneous polynomial of the form

$$\Psi(\boldsymbol{S}) = [G_n(\boldsymbol{S})]^m \quad \text{such that} \quad m = \frac{k}{n}. \tag{4}$$

The degree n of the homogenous polynomial $G_n(\boldsymbol{S})$ is always a positive even number. For such plastic potentials, the rate of the plastic work per unit volume ($\dot{W}$) is found to be equal to Ψ. Equation 3 is similar to a conventional power

law showing that the strain rate increases with the $(k-1)^{th}$ power of the stress magnitude. On comparison of Equation 3 to a stress-strain rate relationship of the type $\sigma \propto D^{\mu}$, the physical meaning of k is given by $k = (1+\mu)/\mu$, where μ represents the strain rate sensitivity exponent. According to the Facet approach [34], the homogeneous polynomial $G_n(\boldsymbol{S})$ can be chosen to be of the form

$$G_n(\boldsymbol{S}) = \sum_{\kappa=1}^{K} \lambda_\kappa (d_{\kappa p} S_p)^n = \dot{W}^{\frac{1}{m}} \quad \text{with} \quad \lambda_\kappa \geq 0. \tag{5}$$

Here, K corresponds to the number of strain rate modes (unit strain rate vectors) imposed on a CP derived model to fit the parameters λ_κ and $\boldsymbol{d}_\kappa$. It must be noted that $\boldsymbol{d}_\kappa$ refer to the imposed plastic strain rate vectors to calibrate the plastic potential function but not the global plastic strain rate defined in Equation 2. Also, $d_{\kappa p}$ and S_p denote the components of the 5D deviatoric vectors $\boldsymbol{d}_\kappa$ and $\boldsymbol{S}$ (Einstein summation over p), respectively. As the value of $n \to \infty$, the plastic potential function becomes more faceted with sharp vertices (less rounded) and has much closer resemblance to a single crystal yield surface. For a rate-insensitive material with strain rate sensitivity exponent $\mu \to 0$, i.e. $\frac{1}{m} \to 0$, the mathematical description of the yield locus can be written from Equation 5 as

$$G_n(\boldsymbol{S}) = 1. \tag{6}$$

To identify the function $G_n(\boldsymbol{S})$, the parameters λ_κ must be fitted using a large number of plastic strain rate and yield stress pairs ($\boldsymbol{d}_\kappa$ and $\boldsymbol{S}_\kappa$) derived from a strain driven CP model for a nearly equidistant grid in stress space.

Here, we have developed an alternative method, aimed specifically at obtaining the function $G_n(\boldsymbol{S})$ for single crystals. Let us now consider the yield surface of a single crystal with just one slip system (κ). The yield surface would then be given by the Generalized Schmid law as

$$\boldsymbol{M}_\kappa : \boldsymbol{\sigma} = \pm \tau_c \quad \text{with} \quad \boldsymbol{M}_\kappa = \frac{(\boldsymbol{n}_\kappa \otimes \boldsymbol{b}_\kappa) + (\boldsymbol{b}_\kappa \otimes \boldsymbol{n}_\kappa)}{2} \tag{7}$$

where $\boldsymbol{n}_\kappa$ and $\boldsymbol{b}_\kappa$ (unit vectors) denote the slip plane normal and slip directions, respectively. The tensor $\boldsymbol{M}_\kappa$ is symmetric and can be represented as a vector in the 6D stress space and from now on we always refer to its vector form. Here, τ_c is the Critical Resolved Shear Stress (CRSS) and $\boldsymbol{\sigma}$ is the stress tensor in the crystal reference frame. Such an yield locus with just one active slip system would consist of two separate yield surfaces (due to $\pm\tau_c$), which are essentially hyperplanes in the 6D vector space. Note that, here we talk about the whole stress tensor but not the deviatoric stresses, which, for an incompressible material, can be represented in a 5D deviatoric vector space. The resulting expression for the yield locus of such a single crystal with one slip system, in the $XX-YY$ plane is given in Equation 8, and can be represented via Figure 1.

$$M_\kappa^{11}\sigma_{XX} + M_\kappa^{22}\sigma_{YY} = \pm\tau_c \tag{8}$$

It can be shown that for a single crystal with one slip system, the coefficients of such an hyperplane are proportional to the components of the plastic strain rate vector $\boldsymbol{d}_\kappa$. This would also pertain to the normality rule for associated plasticity where the plastic strain rate vector for a point lying on the yield surface, here the hyperplane, is always normal to it. In an alternate sense, a plastic strain rate vector acting normal to the yield surface would essentially activate that particular slip system. Such a plastic strain rate vector can be denoted by

$$\boldsymbol{d}_\kappa = \boldsymbol{M}_\kappa\dot{\gamma_\kappa}. \tag{9}$$

where $\dot{\gamma_\kappa}$ is a measure of the shear strain rate in the slip system. We can thus obtain the plastic strain rate vector corresponding to the activation of a given slip system through Equation 9. For a known number of slip systems in a single crystal, a set of plastic strain vectors that each correspond to the activation of individual slip systems can be determined. The resulting hyperplanes corresponding to all these vectors would eventually define the convex yield surface of a single crystal in the 6D vector space, with the yield locus looking much similar to that of a "6D facet eye" with sharp vertices. Along this line of motivation,

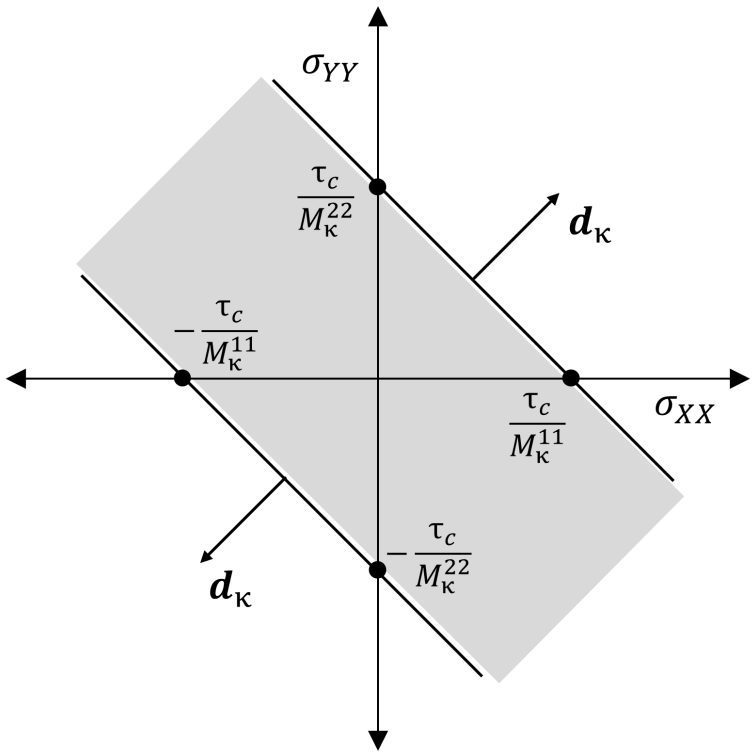

Figure 1: The yield locus of a single crystal with one slip system defined by Equation 8. The normal plastic strain rate vectors are denoted by $\boldsymbol{d}_\kappa$.

we utilize these exact plastic strain rate vectors that activate the slips systems of a single crystal to derive the Facet plastic potential function. The test plastic strain rates $\boldsymbol{d}_\kappa$ of Equation 5 that calibrate the plastic potential function are replaced by those from Equation 9 that correspond to the activation of each of the slip system in a given single crystal. The number of terms in the resulting Facet expression is thus equal to the number of slip systems in the given crystal structure. As per the Taylor theory [20] for plastic strain in metals, the frictional power dissipated or the work done in the activation of a single slip system κ can be represented by the work conjugate of the CRSS and slip system shear strain rate, $\dot{\gamma}_\kappa$. Hence, the function $G_n(\boldsymbol{S})$ of a single crystal plastic potential

in terms of the work normalized plastic strain rates, is given by

$$\sum_{\kappa=1}^{s} \lambda_\kappa (d^w_{\kappa p} S_p)^n = 1. \tag{10}$$

where s denotes the number of slip systems in a single crystal and $d^w_{\kappa p}$ are the work normalized strain rate vector components in the deviatoric strain rate space. In the above equation, the work normalized strain rate vectors are

$$\boldsymbol{d}^w_\kappa = \frac{\boldsymbol{M}_\kappa \dot{\gamma_\kappa}}{\dot{W}_\kappa} \quad \text{with} \quad \dot{W}_\kappa = \tau_c \dot{\gamma_\kappa}. \tag{11}$$

Since work normalized strain rate vectors corresponding to the single crystal slip systems are used, the values of the parameters λ_κ can be taken as 1 for all the terms in Equation 10 (equal weight assignment to each slip system). Such a Facet expression, for large values of n (say $n > 20$) will result in a faceted single crystal yield locus.

The xx-yy yield section of the FCC single crystals for different values of n, generated from the Facet plastic potential are presented in Figure 2. The slip systems under consideration are $\{111\}\langle 110\rangle$. It can be immediately realized that the increase in the order of the Facet expression makes the yield locus section from the plastic potential more akin to the theoretical yield locus section. Since the vertices of the facets are rounded, the common issue associated with the determination of the plastic strain rate direction at the vertex in rate-independent CPFEM calculations is avoided as well.

In an earlier work in literature [36], a similar analytical expression for the single crystal yield locus of FCC crystals involving an exponent was also derived. However, the authors had utilized the Generalized Schmid law (Equation 7) to derive flow surface as an inner envelope of the resulting hyperplanes from all the slip systems combined. A hypersurface was derived from homogeneous functions of degree 1 (each from a hyperplane), with a real exponent, the increase in value of which led to a closer resemblance to the actual yield locus.

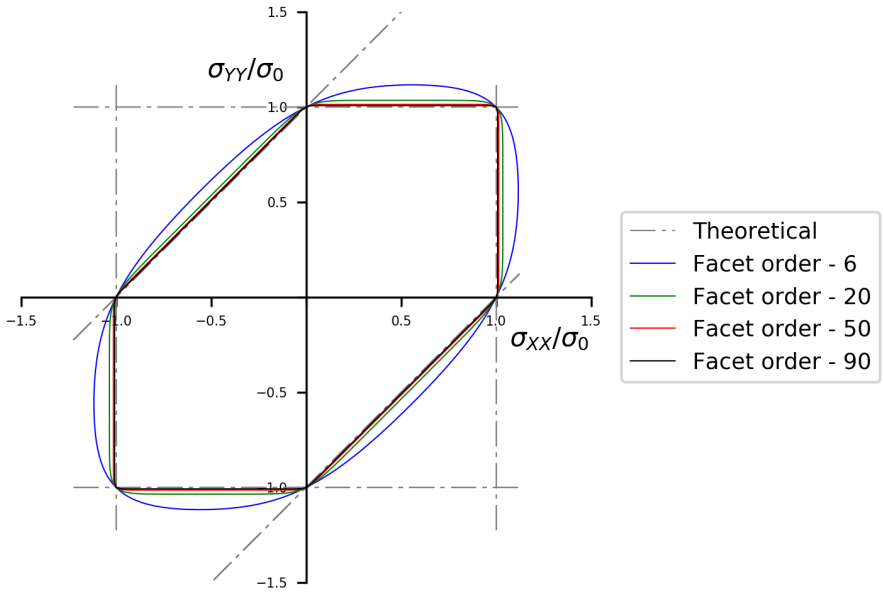

Figure 2: Theoretical (enclosed by the dash-dot lines) and Facet derived yield section (continuous lines) of the FCC single crystals with stress components (σ_{XX} and σ_{YY}) normalized with the uniaxial yield stress (σ_0). The yield section corresponds to crystals with a crystal reference frame coinciding with the global reference frame.

2.2. Meso-scale: FE model of the multi-phase RVE

2.2.1. RVE construction

The meso scale FE simulations are performed on an RVE capable of representing the underlying microstructure in sufficient detail. Features such as morphological distribution of phases, phase volume fraction, grain sizes and shapes, lattice orientations etc. can be included in the microstructure. The construction of the RVE is done in Dream3D (an open source microstructure generation software [10]). Dream3D facilitates the digital reconstruction of 3D microstructures or the translation of statistical material characterization parameters into a representative microstructure (Figure 3). The former can be achieved via full topological microstructural representations (like 2D serial EBSD sections) while the latter utilizes distribution functions of grain size and aspect ratios, phase composition and orientation distribution function to generate synthetic

microstructures. The microstructures generated can be periodic in nature too. The output from Dream3D can be obtained as Abaqus input files of the FE mesh with elements grouped together into several domains (referred to as "model section" within the Abaqus environment) that each represent an individual grain. An additional file containing the orientation of the grains as Euler angles along with the phase information is also generated. A Python script is then used to import the input files and assign phase specific material properties and orientations to different grains in the microstructure, and finally set up Abaqus simulations with appropriate boundary conditions.

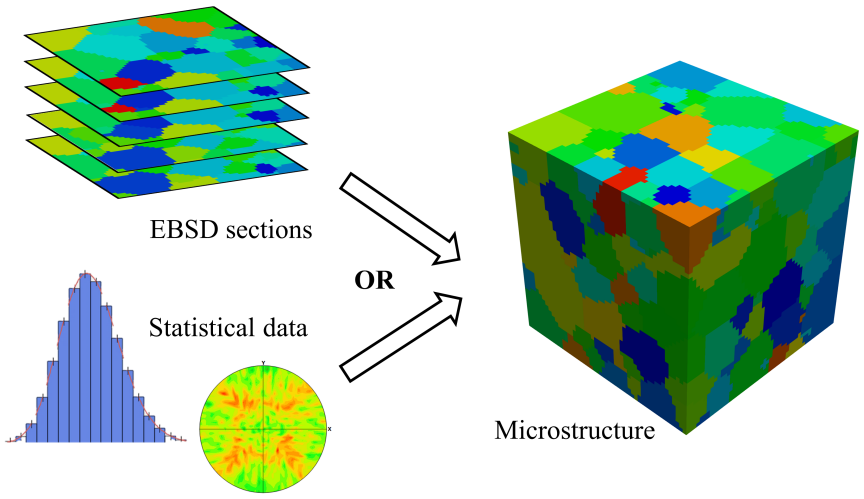

Figure 3: Microstructure construction using Dream3D from EBSD maps or statistical distributions such as grain size distribution and pole figure. Please note that the above figure is a mere graphical illustration of the actual microstructure generation process, and does not refer to the microstructure used in further simulations.

2.2.2. FE simulations

The FE simulations are performed in Abaqus using an explicit user material subroutine (VUMAT) within the Hierarchical Multiscale (HMS) software [21]. The Abaqus FE mesh consists of several domains with groups of elements (Abaqus model sections), each representing a specific grain in the microstruc-

ture. The Euler angle information of each grain, obtained from Dream3D, is attached as a local reference frame to the corresponding grain section (Abaqus material orientations). This ensures that the transformation of stresses/strains from the global to the local reference frame of the VUMAT is performed inherently by Abaqus. However, sufficient care must be exercised in analyzing the Abaqus results from the FE simulations, as the stress and strain tensor outputs are always returned with respect to the local (grain) reference frame. A unique phase ID is assigned to every integration point in the FE mesh using the information about the phase to which a given grain belongs to, and this is eventually utilized within the VUMAT to choose the appropriate phase specific plastic potential function.

The HMS based VUMAT adopts a stress integration algorithm based on the formulation of "Elastic Predictor-Plastic Corrector (Radial return mapping) [49]" at every explicit time step. The algorithm calculates an elastic trial stress using the fourth-rank elasticity tensor at the start of the time increment, followed by a plastic correction, such that the final stress tensor lies approximately on the yield locus. A brief summary of the steps involved in the calculation of the stress increments via the VUMAT is provided here. For a typical time increment, the quantities before and after the time step are denoted by the superscripts $^{(t)}$ and $^{(t+\Delta t)}$, respectively. The trial stress for an explicit time step is

$$\boldsymbol{\sigma}^{tr} = \boldsymbol{\sigma}^{(t)} + \mathbb{C}^e : \Delta\boldsymbol{\varepsilon}, \tag{12}$$

where $\mathbb{C}^e$ is the fourth order elastic tangent modulus. The onset of yield is assessed through a positive scalar value α such that $\boldsymbol{\sigma}^{tr}/\alpha$ lies on the yield surface. Ideally, $\alpha \leq 1$ for an elastic time increment and $\alpha > 1$ for a plastic time increment. For the latter, the stress at the end of the time increment can be obtained through a plastic correction to the trial stress by means of the

incremental plastic strain $\Delta\boldsymbol{\varepsilon}^p$ as

$$\begin{aligned}\boldsymbol{\sigma}^{(t+\Delta t)} &= \boldsymbol{\sigma}^{(tr)} - \mathbb{C}^e : \Delta\boldsymbol{\varepsilon}^p \quad \text{with} \\ \Delta\boldsymbol{\varepsilon}^p &= \Delta\varepsilon^p \hat{\boldsymbol{D}}_p.\end{aligned} \tag{13}$$

Here, $\hat{\boldsymbol{D}}_p$ is the unit vector in the plastic strain rate direction or the plastic strain rate mode. The plastic strain increments are eventually determined using the phase specific plastic potential functions as follows. From the concept of work conjugates, the rate of plastic work per unit volume done can be defined as

$$\dot{W} = \boldsymbol{\sigma} : \boldsymbol{D}_p = \sigma^{eq} D_p^{eq}, \tag{14}$$

with the incremental form of the same being

$$\Delta W = \boldsymbol{\sigma}^{(t+\Delta t)} : \Delta\boldsymbol{\varepsilon}^p = \sigma^{eq\ (t+\Delta t)} \Delta\varepsilon^{eq} \tag{15}$$

where σ^{eq}, D_p^{eq} and $\Delta\varepsilon^{eq}$ are the equivalent stress, equivalent plastic strain rate and equivalent plastic strain, respectively. A deviatoric stress mode $\hat{\boldsymbol{S}}$ of the trial stress, of unit magnitude, is defined as

$$\hat{\boldsymbol{S}} = \frac{\boldsymbol{S}}{\|\boldsymbol{S}\|}. \tag{16}$$

Using the plastic potential function defined in terms of the above stress mode ($\Psi(\hat{\boldsymbol{S}})$), the plastic strain rate mode can be obtained as

$$\hat{\boldsymbol{D}}_p = \frac{1}{\|\boldsymbol{D}_p\|} \frac{\partial \Psi(\hat{\boldsymbol{S}})}{\partial \hat{\boldsymbol{S}}}. \tag{17}$$

Further a scaled plastic potential function is also defined for numerical convenience, as given in:

$$\psi(\hat{\boldsymbol{S}}) = \frac{\hat{\boldsymbol{S}} : \hat{\boldsymbol{D}}_p}{\Psi(\hat{\boldsymbol{S}})}. \tag{18}$$

The incremental relations of the equivalent strain and equivalent stress are shown in the equations below. The latter is the linearized form of the grain hardening law with $\mathbb{H}$ as the hardening modulus, as shown below:

$$\begin{aligned} \Delta\varepsilon^{eq} &= \Delta\varepsilon^{p}\psi^{(t)}(\hat{\boldsymbol{S}}) \\ \sigma^{eq\ (t+\Delta t)} &= \sigma^{eq\ (t)} + \mathbb{H}^{(t)}\ \Delta\varepsilon^{eq}. \end{aligned} \tag{19}$$

Combining Equations 13, 15 and 19, the incremental plastic strain can immediately be derived from the relation:

$$\Delta\varepsilon^{p} = \frac{\boldsymbol{\sigma}^{(tr)} : \hat{\boldsymbol{D}}_p - \sigma^{eq\ (t)}\psi^{(t)}(\hat{\boldsymbol{S}})}{\mathbb{H}^{(t)}[\psi^{(t)}(\hat{\boldsymbol{S}})]^2 + (\mathbb{C}^e : \hat{\boldsymbol{D}}_p) : \hat{\boldsymbol{D}}_p}. \tag{20}$$

The stress tensor at the end of the time increment can thus be calculated from Equation 13 using the above relation. At each integration point for which the VUMAT is evaluated, the corresponding phase specific plastic potential function is provided as input.

2.2.3. Boundary conditions

For microstructural simulations, the usage of periodic microstructures coupled with Periodic Boundary Conditions (PBCs) would provide a better estimate of the effective properties [50, 51], and hence the usage of the same is more common nowadays. In this section, we have implemented the prescription of PBCs within the Finite Element set up of the developed model for 3D RVE simulations. Eventually, we have also extended the same formulation to impose specific stress states on the RVE. In principle, the reaction forces on the faces of the RVE are controlled throughout the course of the simulation such that the RVE Cauchy stress tensor is always directed along a desired path. The ability to impose such stress BCs would help construct the yield locus from our microstructure simulations. This has been demonstrated in the following sections of the article.

The prescription of nodal displacements or forces as Boundary Conditions (BCs) is possible within a general FE framework. For displacement driven simulations, it is possible to define the macroscopic deformation gradient history in

the form of PBCs. In general, periodicity in BCs for two faces with translational symmetry can be represented as

$$\boldsymbol{x}^j - \boldsymbol{x}^0 = \boldsymbol{F}(\boldsymbol{X}^j - \boldsymbol{X}^0). \tag{21}$$

Here the index j represents the pair of opposite faces (congruent faces) containing nodes with a pure translational symmetry along the global reference axes. $\boldsymbol{X}$ and $\boldsymbol{x}$ are the position vectors at the initial and final configurations, respectively, with $\boldsymbol{F} = \mathbf{1} + \boldsymbol{\nabla u}$ being the large strain deformation gradient tensor. L is the geometrical dimension of a regular cubic RVE. For such a $3D$ RVE, the displacement on the opposite faces of the RVE can be expressed as

$$u_i^j - u_i^0 = L\ \nabla u_{ij} \quad with \quad i, j = 1\ to\ 3. \tag{22}$$

The above equations can be set up within the FE framework in Abaqus through the introduction of 3 dummy nodes (at a distance from the faces of the RVE), along the 3 coordinate axes with Degrees Of Freedom (DOFs) i. This can be established via linear constraint equations where the DOFs of the nodes on the congruent faces are tied to the DOFs of the dummy nodes such that the displacements of the latter would eventually represent the components of the displacement gradient shown in Equation 22. It is worth taking note of that the dummy nodes are essentially ghost nodes that do not have any physical motivation, rather, merely exist as a numerical technique to impose the PBCs. Also, sufficient constraints were defined to prevent the rigid body translation and rotation of the RVE. It is essential to set up additional constraint equations for the nodes on the corners and edges of the $3D$ RVE in order to avoid redundant conditions resulting from the equations on the common nodes on adjacent faces. Otherwise, the dependent boundary constraints on shared nodes will result in inconsistencies in Abaqus FE simulations [52]. It can be accomplished by establishing a "master-slave" set of nodal constraint equations, in line with Equation 22. A graphical representation of one such case, for the edge nodes of a cubical RVE parallel to the Z axis, is shown in Figure 4. The master edge is

represented as 1, while the slave edges are represented by 2, 3 and 4. The superscript denotes the edges to which the nodes belong to while the subscripts X and Y of the ∇u term represents the perpendicular axes to the pair of opposite faces whose displacement gradient terms are utilized. The index i is the DOFs of the nodes.

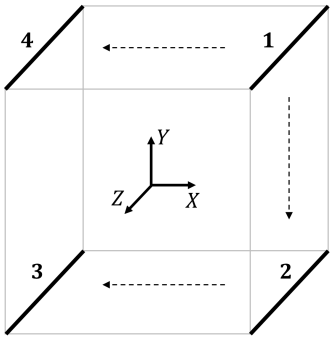

$$
\begin{aligned}
u_i^2 - u_i^1 &= L\ \nabla u_{iY} \\
u_i^4 - u_i^1 &= L\ \nabla u_{iX} \\
u_i^3 - u_i^1 &= L\ \nabla u_{iY} + L\ \nabla u_{iX}
\end{aligned}
\tag{23}
$$

Figure 4: Figure showing an edge set consisting of edges parallel to the Z axis.

Further, the implementation of stress BCs is done using the relation between the element nodal reaction forces and the first Piola-Kirchoff stress tensor (also known as the Nominal stress tensor)($\boldsymbol{P}$), defined by the Cauchy stress tensor ($\boldsymbol{\sigma}$) and the deformation gradient tensor ($\boldsymbol{F}$). The stress tensor $\boldsymbol{P}$, a measure of the force acting on an element in the final configuration divided by the area of the respective element in the initial configuration is related to $\boldsymbol{\sigma}$ as

$$
\boldsymbol{P} = |\boldsymbol{F}|\boldsymbol{\sigma}\boldsymbol{F}^{-T}. \tag{24}
$$

It must be insisted that despite the Cauchy stress being symmetric, the first Piola-Kirchoff stress is not symmetric. The reaction forces on the element nodes can then be established as

$$
R_i^K = A\ P_{iK}. \tag{25}
$$

where R_i^K and A are reaction forces on the K^{th} dummy node located along

the global coordinate axis and the the area of the RVE face over which the force acts, respectively. The numerical set up within Abaqus to load the RVE along specific stress paths can be achieved by defining a dummy user element (User subroutine: VUEL), composed of the three dummy nodes carrying the PBCs, where the nodal reactions forces of the element are set up via Equation 25. Thus, the DOFs of the dummy nodes and in turn the dummy element are tied implicitly to the DOFs of the nodes on the congruent faces of the RVE boundary via the constraint equations. The user element contribution to the external force vector in the global FE system of equations is formulated in terms of the Cauchy stress state $\boldsymbol{\sigma}$ to be imposed on the RVE, as in Equations 24. The Cauchy stress paths can then be specified as input parameters to the user element.

2.3. Macro-scale: Homogenized RVE response

The macroscopic material response of the meso-scale microstructure is obtained through a homogenization procedure. Since the FE output is obtained at discrete integration points, the homogenized response can be calculated by volume averaging the quantities over the domain of interest. The RVE response can thus be calculated by

$$\boldsymbol{\zeta}_{RVE} = \frac{1}{V_{RVE}} \left\{ \sum_{phases} \left\{ \sum_{grains} \left\{ \sum_{nodes} \boldsymbol{Q}^{-1} \boldsymbol{\zeta}_{node} \boldsymbol{Q}^{T^{-1}} * V_{node} \right\} \right\} \right\}. \quad (26)$$

Here V_{node} and V_{RVE} denote the volume associated with each node ($1/8^{th}$ of an eight node brick element volume) and the total RVE volume, respectively. The rotation matrix $\boldsymbol{Q}$, constructed from the Euler angle orientation of a given grain, is used to transform the tensor $\boldsymbol{\zeta}$ from the local reference frame (of a grain) to the global reference frame. The individual phase and grain averaged response can also be extracted via the same procedure.

3. Material and Methods

3.1. Microstructure of Duplex steel

The numerical simulations were performed on the synthetic Duplex steel microstructure shown in Figure 5. The RVE was constructed using statistical parameters extracted from literature [40], for commercial Duplex Stainless Steel, and hence the same shall be considered as reference material to evaluate the model predictions. The volume fractions of austenitic and ferritic phases were 0.42 and 0.58, respectively. The grain size distributions for the individual phases were chosen such that the average grain sizes of the former and the latter were 5.0 μm and 9.0 μm. The resulting sizes of the equiaxed grains vary over a range of 4.5-5.5 μm for austenite and 7.0-11.0 μm for ferrite, and were distributed such that the resulting RVE was periodic in nature. The grain orientations were assigned in a random manner without any specific strong texture components akin to the reference literature [40]. The RVE, of size $80 \times 80 \times 80$ μm^3, consisted of ~ 2400 grains. The dimensions of the RVE were chosen such that there were comparable number of grains with respect to the reference material with a wide range of grain sizes.

Figure 5: RVE showing the distribution of the grains in the synthetic microstructure. Grain distribution and their boundaries are depicted by the color overlay.

The material laws for the phases in the RVE were defined via single crystal Facets derived from the procedure established in Subsection 2.1. The slip systems chosen for the austenitic and ferritic phases were that of the typical FCC and BCC single crystals. The slip systems under consideration for the FCC and BCC single crystals were $\{111\}\langle 110\rangle$ and $\{110\}\langle 111\rangle + \{112\}\langle 111\rangle$, respectively. A higher order plastic potential function was able to capture the faceted nature of the yield locus, and here an order of 50 was used for the simulations. The resulting yield loci for both the phases are plotted along the XX-YY plane in Figure 6. The yield stresses were normalized with respect to the uniaxial tensile yield stress (σ_0) and the plotted sections correspond to crystals with reference frames oriented along the global reference frame of the FE mesh. The choice of the CRSS for each phase is not significant as they do not explicitly enter into the calculations since the yield locus is always normalized with respect to the yield stress from uniaxial tension. In principle, the plastic potential function provides the shape of the yield locus while the hardening law acts as a scaling factor on the yield locus during plastic time increments. The hardening behavior of the individual grains was given by a phase specific isotropic Swift hardening law defined as a function of von Mises equivalent strain in the crystal, operating at the level of individual grains in the RVE. The parameters of the grain hardening law were fitted through iterative numerical simulations of tensile tests performed on the RVE. The initial parameters of the grain hardening law for the fitting simulations were obtained from the phase flow curves available in literature for the CPFEM simulations on the reference Duplex Stainless Steel microstructure [40]. The differences between the predicted phase flow curves from the simulation and the reference phase flow curves were then applied as correction to the grain hardening law input for the subsequent iterations. The process was repeated until reasonable predictions were obtained for the phase flow curves. The anisotropic single crystal elastic constants (matrix components c_{ijkl} of the fourth order tangent modulus in the crystal reference frame) [40] and hardening law parameters of individual phases used in the simulations are summarized in Table 1.

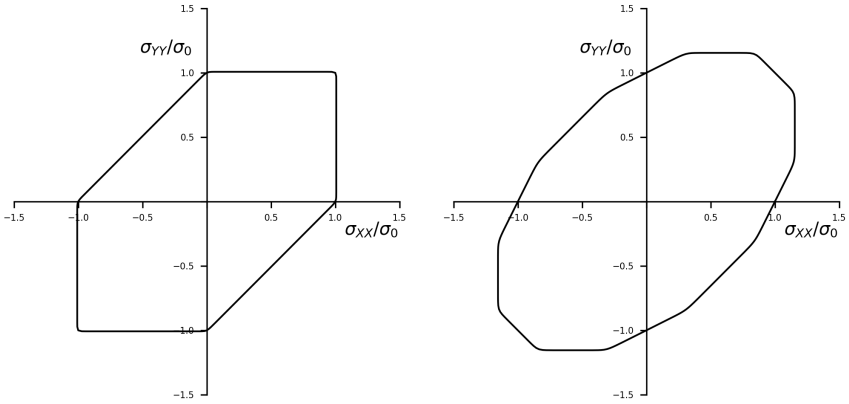

Figure 6: The normalized XX-YY yield sections of the individual phases used in the simulation, Austenite (left) and Ferrite (right), derived from a Facet plastic potential of order 50.

The FE mesh of the RVE consists of $40\times40\times40$ eight node brick elements (of C3D8 type in Abaqus), with the dimension of each element being $2\times2\times2$ μm^3. The RVE mesh discretization was coarse enough to capture the average grain size of the equiaxed grains in the individual phases obtained from literature [40], while remaining computationally efficient. The Abaqus FE model represented in Figure 7 shows the phase distribution within the microstructure. The imposed loading rate during the explicit time step was controlled such that the simulations were well within the quasi-static regime, i.e. the ratio of kinetic energy to total energy was less than 1%. The Abaqus computations with PBCs (through additional constraints imposed on the FE model) took ~ 2.5 hours for completion, using an Intel Xeon processor without parallelization.

3.2. Tensile test simulation

Numerical simulation of a displacement controlled uniaxial tensile test was performed on the RVE by applying PBCs. The displacement boundary conditions of the tensile test, for three pairs of opposite faces of the FE mesh are shown

[1] $\sigma^{eq} = K(\varepsilon_0^{eq} + \varepsilon^{eq})^n$, σ^{eq} & ε^{eq} are the equivalent stress and effective plastic strain, respectively.

Material properties	**Austenite**	**Ferrite**
Density (kg/m^3)	7800	7800
c_{iiii} (GPa)	197.5	231.4
$c_{iijj}(i \neq j)$ (GPa)	124.5	134.7
$c_{ijji} = c_{ijij}(i \neq j)$ (GPa)	122	116.4
Swift hardening law parameters[1]		
K (MPa)	1345	1796
n	0.4347	0.3370
ε_0^{eq}	0.1133	0.0540

Table 1: Macroscopic material parameters [40] of individual phases used in Abaqus simulations.

in Table 2. The applied displacement is imposed as a smooth function over time. Additional BCs to prevent rigid body translation and rotation were also defined.

Uniaxial tension along X direction		
RVE faces ∥ YZ plane:	RVE faces ∥ XZ plane:	RVE Faces ∥ XY plane:
$u_1^L - u_1^0 = 10\ \mu m$	$u_1^L - u_1^0 \neq 0$	$u_1^L - u_1^0 \neq 0$
$u_2^L - u_2^0 = 0$	$u_2^L - u_2^0 \neq 0$	$u_2^L - u_2^0 \neq 0$
$u_3^L - u_3^0 = 0$	$u_3^L - u_3^0 = 0$	$u_3^L - u_3^0 \neq 0$

Table 2: PBCs for the uniaxial tensile test simulation. The constraint equations with a RHS value of 0 were imposed to prevent rigid body motions.

3.3. Virtual diffraction simulation

As a test to validate the method on phase level, virtual diffraction experiments were conducted on the synthetic duplex steel microstructure to measure the lattice strains, for further comparison with the experimental data in the reference literature [40]. The RVE was subjected to tension along X direction

Figure 7: Abaqus Finite Element mesh showing the phase distribution in the RVE. Austenite and ferrite grains are colored green and white, respectively.

using the same BCs as in Table 2. The diffraction calculations were then performed through a post processing routine set up in Python. The diffraction vector ($\hat{\boldsymbol{k}}$) was aligned along the loading direction. In order to select the grains that contribute to a diffraction signal in the given direction, for a given grain, the normal to the specific diffraction plane was rotated from the local reference frame ($\hat{\boldsymbol{n}}_{grain}$) to the global reference frame ($\hat{\boldsymbol{n}}_{global}$) via the Euler rotation matrix ($\boldsymbol{Q}$), as shown below

$$\hat{\boldsymbol{n}}_{global} = \boldsymbol{Q}^{-1} \cdot \hat{\boldsymbol{n}}_{grain}. \tag{27}$$

If the angle between the vectors $\hat{\boldsymbol{n}}_{global}$ and $\hat{\boldsymbol{k}}$ lies within the chosen angle spread (here 6.5° was used in line with the experimental data used for evaluation), then that particular grain was said to contribute to the diffraction peak. The volume averaged lattice strain of the respective grains was then compared with the experimental results [40]. It should be noted that the lattice strains were calculated from the total and plastic strain values from the numerical simulation, which were written into State Dependent Variables (SDVs) from the Abaqus VUMAT during the simulation. The diffraction planes studied include (200),

(311) and (111) for the austenitic phase, and (200) and (211) for the ferritic phase.

3.4. Yield locus prediction

A numerical procedure to construct the anisotropic yield locus of multi-phase microstructures is presented below. The RVE is loaded into specific stress (true stress) states, using the stress based PBC framework explained in Subsection 2.2. Here, the stress path or the stress mode [53], has the meaning of a unit vector (which in reality is a tensor), pointing towards a specific direction in the $6D$ stress space. The point on the yield locus in the direction specified by a stress mode $\hat{\boldsymbol{Y}}$ is given by

$$\boldsymbol{\sigma}_y = \sigma_y \hat{\boldsymbol{Y}}. \tag{28}$$

σ_y is the distance from the origin to the point on the yield locus, in the direction of the stress mode (Figure 8).

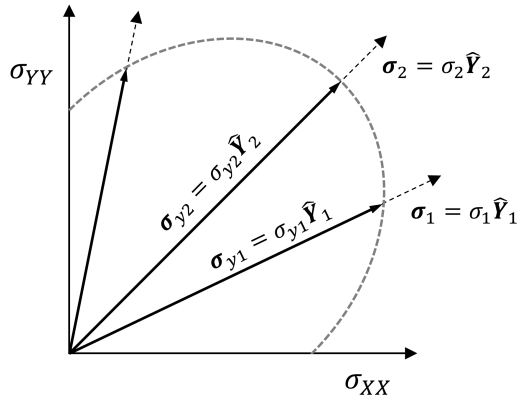

Figure 8: A yield section on the xx-yy plane showing the stress modes $\hat{\boldsymbol{Y}}$ for different stress states.

In an earlier work [54], a method to define a stress-strain curve for multi-axial

stress state was provided. For a multi-axial stress mode of the form

$$\boldsymbol{\sigma} = \sigma \hat{\boldsymbol{Y}}, \tag{29}$$

it is possible to define a scalar variable ε_p from the total plastic strain rate $\dot{\boldsymbol{\varepsilon}}_p$ as

$$\varepsilon_p = \int_0^t \hat{\boldsymbol{Y}} : \dot{\boldsymbol{\varepsilon}}_p \, dt. \tag{30}$$

The scalars σ and ε_p represent a work conjugate pair. A stress strain curve, as shown in Figure 9, can be constructed using these scalar variables corresponding to the imposed multi-axial stress state.

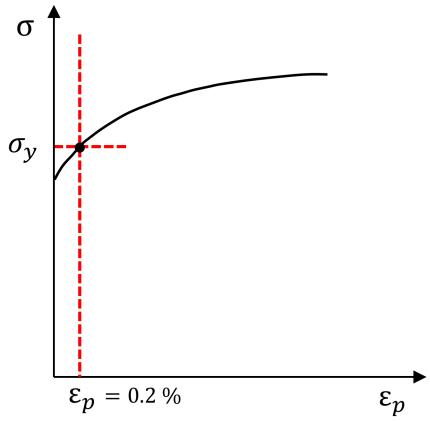

Figure 9: Yield stress vs. plastic strain curve showing the yield point for a multi-axial stress state.

From such a curve, the onset of yield can be deduced as the point σ_y where there is a transition from the linear to the non-linear part. A conventional offset plastic strain of 0.2% (similar to the $R_{p0.2}$ offset yield strength adopted in industrial standards) is considered to denote the transition from the elastic to plastic regime for our calculations. To describe the yield locus along a specific section, say $XX - YY$, a series of stress modes separated by a constant angle, lying on that particular section can be imposed as BCs for the FE simulations.

Here, as shown in Figure 10 and Equation 31, stress modes obtained by changing the value of θ such that $0° \leq \theta \leq 90°$ with a spatial resolution of 5°, were defined.

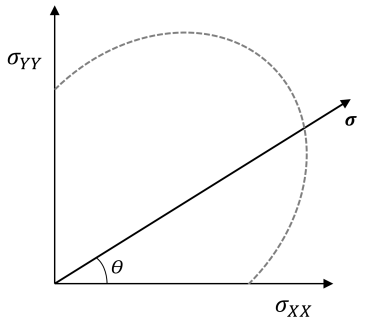

$$\boldsymbol{\sigma} = \sigma \begin{pmatrix} cos\theta & 0 & 0 \\ 0 & sin\theta & 0 \\ 0 & 0 & 0 \end{pmatrix} \quad \text{with} \quad \sigma = 1200 \text{ MPa}. \tag{31}$$

Figure 10: Figure showing a stress mode at an angle θ to the X axis.

Sufficient care must be taken in choosing the magnitude of the stress tensor σ (= 1200 MPa for all the stress modes), as it is essential that the RVE is loaded well beyond the yield stress for all angles θ. From the homogenized RVE responses for different stress states, stress strain curves as in Figure 9 can be constructed, from which points lying on the yield locus section can be identified.

4. Results and Discussion

4.1. Tensile test simulations

The homogenized response of the RVE was used to construct flow curves of the microstructure along with those of the individual phases. The phase flow curves are obtained from the homogenized response of the grains embedded in the microstrcuture. The calculated flow curves are plotted in Figure 11 along with the experimental stress-strain data procurred from literature [40], for an uniaxial tensile test performed on the reference Duplex Stainless Steel. It is worth mentioning that the displacement applied on the RVE was such that the true strain values from the simulation are sufficient enough and well within the available range of experimental data from the reference literature for comparison.

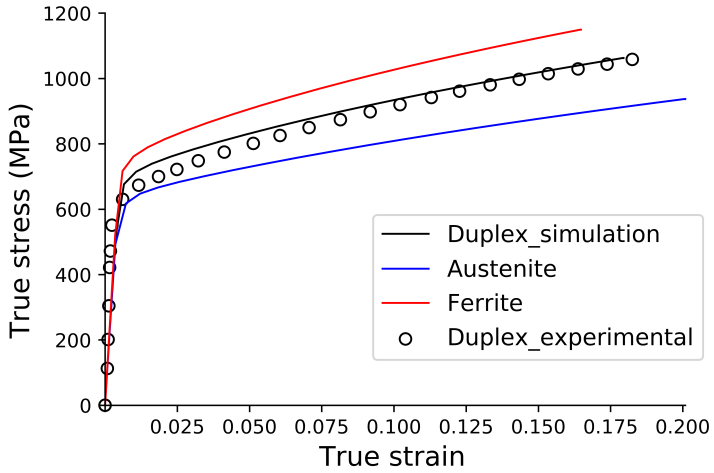

Figure 11: The flow curves of the RVE and individual phases plotted alongside the experimental data of the reference material [40].

The simulated stress-strain curve was in good agreement with the experimental data for strain values > 0.05. At lower strains, although the differences were not extremely large, the macroscopic stresses from the simulations depicted small deviations from the experimental curve. The RVE flow stresses were a non-linear combination of that of the phases and hence, the calibration of the individual grain hardening law is significant in obtaining an exact match with the experimental results. This can be done through fitting the hardening law parameters through an iterative procedure [55] or by obtaining actual material data from micromechanical material characterization tests such as micro-pillar compression [56]. It is also worth mentioning that since texture evolution has not been included in the current model, the effect of texture hardening cannot be captured by the current set up. The material response of the RVE is somewhat dominated by the ferritic phase because of the comparatively greater volume fraction. The stiffer behavior of the ferritic grains under deformation is compensated by the comparatively compliant austenitic grains. Hence, the austenitic phase carries a greater proportion of the strains in comparison with the ferritic phase, and vice versa is observed with respect to the

stresses. The strain partitioning between the Duplex steel phases is denoted in Figure 12. There are no extreme differences between the strains carried by the individual phases due to homogeneous phase distribution of grains within the microstructure, which does not result in formation of islands/walled regions of the harder/softer phase.

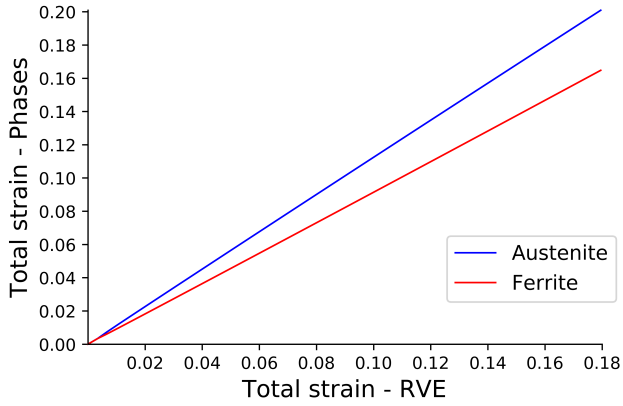

Figure 12: Strain partitioning curves of individual phases in the Duplex steel RVE.

Figure 13 provides an overview of the homogenized equivalent stress-strain behavior of the phases in the RVE, plotted along with the imposed isotropic grain hardening law (Swift law). The continuous lines represent the phase hardening, i.e. the strain hardening in the individual phases of the synthetic microstructure, while the dashed lines are the grain hardening laws defined during the simulation i.e. the hardening curves of free ferrite and austenite. It can be immediately seen that the individual phase hardening is much higher than that of the individual grain hardening curves. The difference between the respective phase hardening curves shows the effect of phase interaction (i.e. grains of the phases). The comparatively coarser and harder ferritic grains undergo much higher strain hardening than the austenitic grains [57]. Also, the deformations in the softer austenitic grains cause stress concentration zones in the harder ferritic phase. Several such zones can be observed in Figure 14, where a YZ section of the deformed synthetic microstructure is depicted. The von Mises

stress is plotted alongside the distribution of phases. The regions of stress hot spots (stress concentration zones) in the ferritic phase are often surrounded by austenitic grains carrying higher strains. Also, the rate of strain hardening, i.e the slope of the strain hardening curves in each phase was considerably different as well.

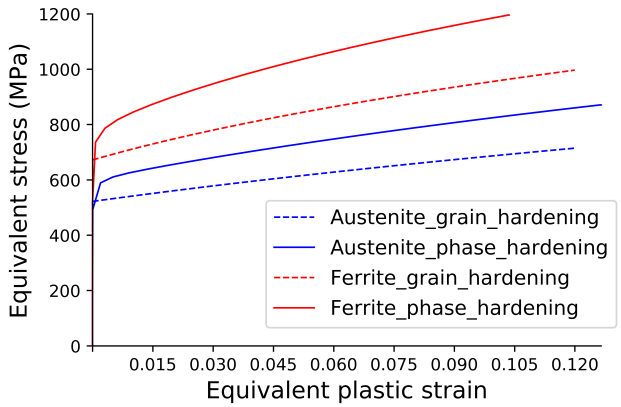

Figure 13: The equivalent stress-strain curves of the phases plotted along with the imposed grain hardening law.

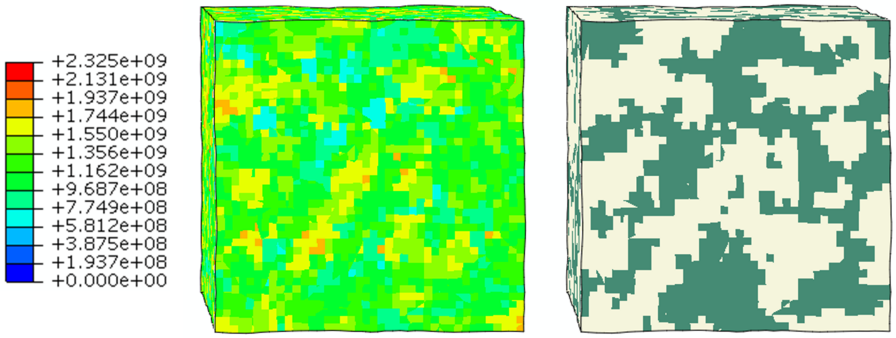

Figure 14: YZ sections of the synthetic microstructure showing the Von Mises stress plot (left) and phase distribution (right). Austenite and ferrite grains are colored green and white, respectively. The stresses are expressed in $N/m^2(Pa)$.

4.2. Virtual diffraction simulations

The lattice strains from the numerical simulations, along the loading direction, are plotted as a function of the macroscopic RVE stresses in Figures 15a and 15b, corresponding to the austenite and ferrite, respectively. The ND experimental data acquired from the reference literature [40] were used for the evaluation of numerical predictions.

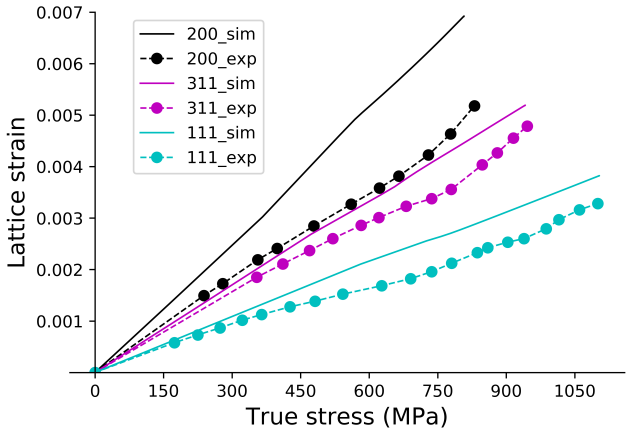

(a) Austenite

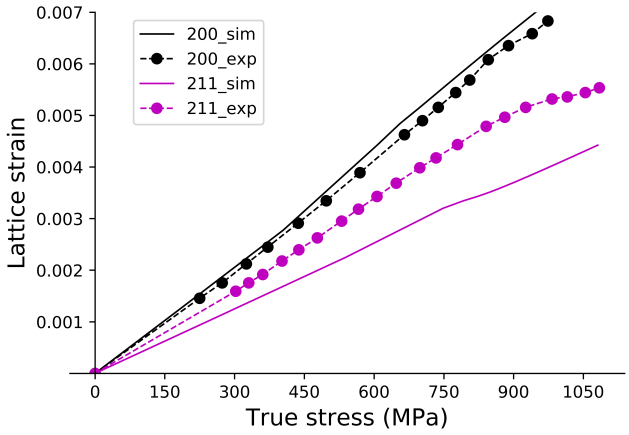

(b) Ferrite

Figure 15: Lattice strains along the loading direction for different diffraction planes plotted as a function of the macroscopic RVE stresses. The simulation and experimental curves [40] in subfigures (a) and (b) are for the austenite and ferrite phases, respectively.

The average number of grains contributing to each diffraction curve for the austenitic and ferritic phases were approximately 12 and 7, respectively. In general, the simulation curves overestimate the lattice strains for the austenitic phase. This is in line with the homogenized flow curves depicted in Figure 11, where at lower strains, the macroscopic flow stresses were underpredicted as well. Due to the lack of a definite transition from the elastic to plastic response, the onset of yield in a lattice plane is located typically at an offset plastic strain value, $\varepsilon_p = 0.2\%$. The adopted yielding condition is also coherent with the RVE yield locus calculations performed further. It must be noted that the commencement of plastic flow in the simulation curves is very subtle unlike the case of experimental results. The (311) and (111) lattice strains of the austenitic phase were in good agreement in the elastic regime, with their respective yield strengths being $\sim$ 630 MPa and $\sim$ 730 MPa. After the onset of plasticity, there were deviations between the numerical and experimental outputs, which seem to get reduced at higher stress values. The maximum difference among the diffraction curves of the austenitic phase was observed in the case of (200) lattice strains, with yielding at $\sim$ 540 MPa. There are prior instances in literature that report such deviations in the numerical-experimental comparison of the (200) lattice strains belonging to the austentic phase, owing to the lack of precision in experimental measurements with low Bragg intensity [58] or from the resulting creep at higher stresses [59], in Duplex steel with similar phase composition. Nevertheless, the (200) lattice strains from the ferritic phase denote almost an exact match with the experimental observations. Even beyond the commencement of yield ($\sim$ 630 MPa), the slope of the lattice strain plots remain unaffected by the plastic deformation. This could be due to the fact that there was no major redistribution of stresses between the phases/grains, at least for the present diffraction plane. Also, the observation might be an indication of strong work hardening. The plots from the case of (211) lattice strains ($\sim$ 760 MPa) show that the simulation results underpredicted the actual values. This was, however, coherent with the numerical comparisons attempted in the reference literature [40] as well.

Phases	**Austenite**		**Ferrite**
Ratio	E_{311}/E_{200}	E_{111}/E_{311}	E_{211}/E_{200}
Experiments	1.20	1.56	1.23
Simulations	1.45	1.56	1.64

Table 3: Diffraction elastic constant ratios calculated from the lattice strain plots for both the phases. The subscripts denote the diffraction planes.

Despite the inability of the model to capture the sensitive variations observed in the experimental readings of any single diffraction curve, the overall changes in the diffraction elastic constant, until the 0.2% offset plastic strain, of the studied diffraction curves for different diffraction planes were replicated to a good extent in the numerical predictions. From Table 3 containing the ratios of these elastic constants calculated from the lattice strain plots in Figures 15a and 15b, it can be seen that an exact correspondence is observed for the E_{111}/E_{311} ratio of the austenitic phase while the other ratios contained a considerable amount of error. The latter is the manifestation of the deviations reported above for (200) and (211) lattice strains of the austenite and ferrite phases, respectively. It can also be realised that the lattice strain predictions depend on the diffraction planes under consideration. The differences in the lattice strain values for a given stress value implies the preferential onset of plasticity in grains with specific orientations. The comparatively higher lattice strains in the (200) lattice planes of both the phase, for the same stress value, indicate the prior onset of plasticity in their counterparts ((311) and (111) planes of the austenitic phase and the (211) plane of the ferritic phase).

To gain a comprehensive overview of the observed differences in lattice strains, it was also essential to ensure if the factors such as mesh discretization and the total number of grains in the FE model affected the overall quality of the diffraction results, as they are typically critical components from an FE perspective. Thus, three additional RVEs were generated with the following features: (1) an RVE of size $100 \times 100 \times 100$ μm^3 with $50 \times 50 \times 50$ elements and

$\sim$ 4000 grains, (2) an RVE of size $120 \times 120 \times 120\ \mu m^3$ with $60 \times 60 \times 60$ elements and $\sim$ 8600 grains, and (3) an RVE with a finer mesh discretization of the original mesh from Figure 7 containing 125000 elements. These microstructures were then subjected to virtual diffraction experiments, the results of which are presented in Figure 16. It can be immediately seen that larger RVEs, despite having a larger number of grains contributing to each diffraction curve (mesh $100 \times 100 \times 100\ \mu m^3$ has $\sim$ 16 austenite grains and $\sim$ 10 ferrite grains and mesh $120 \times 120 \times 120\ \mu m^3$ has $\sim$ 45 austenite grains and $\sim$ 20 ferrite grains, contributing to the lattice strain measurements), do not significantly affect the observed results (Figures 16a and 16b) for the austenitic (111) plane and the ferritic (211) plane. Nevertheless, for the other cases, with an increase in the grain number (i.e. RVE size) the deviations in the lattice predictions seemed to get reduced. In other words, it is possible to capture the lattice strains in the diffraction planes using a minimal number of grains to a certain extent. However, the minimum grain number can eventually vary for different materials. In addition, the lattice strain predictions obtained from the refined mesh in Figures 16c and 16d are almost identical to that of the initial coarser mesh. The effect of stair-stepping (jagged edges) resulting from the voxel elements are negated while calculating the overall homogenized response of a collection of grains. This is also relevant to recent studies which support the aforementioned observation [60, 32]. Nevertheless, it is essential to state that the effect of mesh refinement can be more pronounced in certain applications (like grain boundary effects). In a general sense, since the adopted mesh size directly correlates to the computational efficiency, it must be selected with care. An investigation of the grain number and mesh size sensitivity is beyond the scope of this article and can be an object of interest for the future.

Another important parameter that needs to be addressed is the choice of an explicit FE Abaqus solver for the developed numerical model. Typically, the usage of implicit solvers for multi-scale simulations with CPFE framework is hugely time consuming and often, not feasible. There can be severe problems related to the numerical convergence of integration algorithms for complex

constitutive material laws in an implicit solver. However, explicit solvers can offer reasonable results for quasi-static deformation modes with sufficiently small time stepping in each increment by negating the need for the computation of consistent tangent moduli. Abaqus has the ability to fix a stable time increment inherently from the minimum element size in the FE model, based on the dilatational wave speed of the underlying material calculated from its stiffness.

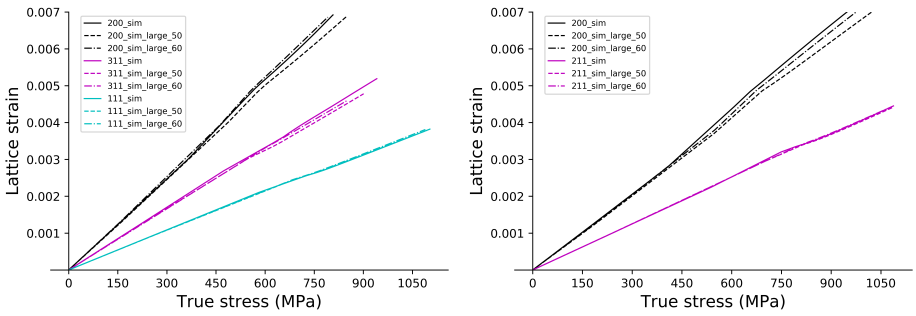

(a) Austenite (b) Ferrite

(c) Austenite (d) Ferrite

Figure 16: Lattice strains along the loading direction for different diffraction planes plotted as a function of the macroscopic RVE stresses. The subfigures (a) and (b) were obtained from RVE simulations of different RVE sizes while subfigures (c) and (d) were from the simulations with different mesh element sizes. In the legend, sim_large_dimension and sim_refined denote a larger RVE and an RVE with finer mesh, respectively.

Also, dynamic explicit analyses can be used for quasi-static problems provided the kinetic energy only represents a small fraction (for example less than 5%) of the total energy. To ensure this, the total time over which the simulations were

performed was sufficiently large enough to negate any dynamic effects. From prior knowledge, such explicit simulations are known to handle elastoplastic material behavior with competence and there are several works that highlight the importance of the same with relevance to CPFEM simulations of complex deformation modes [61, 21, 62]. Hence, it can be stated with confidence that the adopted explicit integration framework does not influence the results of the simulations performed.

On the whole, the observed deviations can primarily be attributed to the difference between the morphology of the actual Duplex Stainless Steel microstructure used as a reference (experimental data from literature) and the synthetic RVE used in simulations, where the former had a complicated banded phase distribution while the latter has a more random distribution of phases. Hence, the intergranular stresses developed within the phases can eventually vary for loading along/across such a morphological alignment. Also, another predominant reason for such variations could be the usage of isotropic grain hardening laws in the present work. There exists no defferential hardening from the mutual interaction of the slip systems and the hardening law parameters are independent of the texture effect. The usage of sophisticated anisotropic grain hardening laws can facilitate parametric fitting based on the simulated diffractions curves, for better correspondence [41, 58]. The experimental evidence from an earlier work on Duplex steel [59] also revealed the dependence of lattice strain evolution on preferential grain orientations, besides their reliance on the elastic and plastic anisotropy. The effect of grain-orientation dependent stresses at the microscopic scale were dominant in the elasto-plastic regime of Duplex steels. In addition, an RVE consisting of larger number of grains contributing to each lattice strain curve seemed to improve the results for specific diffraction planes as well. Since our numerical model does not consider the evolution of texture, the effect of these stresses due to the changes in texture, on lattice strains, are eventually not captured. Also, the issue of preferential orientations or texture, and its evolution is inherently related to the morphology: the higher the volume fraction of a certain orientation of fibre, the higher the chance of connectivity,

and thus lesser impact of weaker or stronger phases included as islands in a connected matrix.

The observed discrepancies thus emphasize the importance of detailed 3D characterization of the actual material along with material specific plasticity mechanisms in order to obtain an accurate material response from the numerical model. Also, for multi-phase steels, such characterization is of paramount importance as the influence of grain-grain and grain-phase interactions play a significant role in determining the overall response.

4.3. Yield locus simulations

A numerical method to construct the anisotropic yield locus from 3D multi-phase RVE simulations was explained in Sections 2.2 and 3.4. Here, a method to construct the yield locus of the Duplex steel RVE using the elaborated procedure is presented. FE simulations to load the meso-scale RVE into specific stress states, with an angular resolution of 5° (Figure 10), were performed. The flow curves (σ-ε_p) extracted from these numerical experiments are presented in Figure 17. The maximum magnitude of the imposed stress tensor was constant for all the simulations. There are also earlier works in literature that construct such flow curves as a function of the total plastic slip [63]. However, in our work, we use the plastic strain measure (ε_p from Equation 30) for the same purpose, since it is more aligned towards the macroscopic scale. On the onset of plasticity, the stress tensor ($\boldsymbol{\sigma}_y$) is calculated using Equation 28. It needs to be emphasized that the choice of the offset strain value would eventually influence the shape of the yield locus and hence, sufficient care must be exercised in choosing the appropriate value of interest.

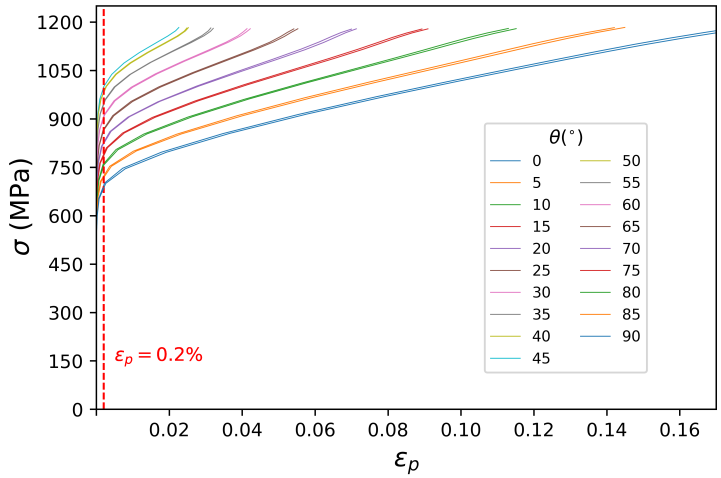

Figure 17: Flow curves extracted from RVE simulations for different stress directions in the XX-YY plane. The θ value here represents the angular resolution of the stress mode (Equation 31) with respect to the global X direction.

The initial yield locus ($\varepsilon_p = 0.2\%$) constructed along the XX-YY plane of the Duplex steel RVE is given in Figure 18. An absence of perfect symmetry (yet negligible) about the $\sigma_{XX} = \sigma_{YY}$ line is manifested and ascribed to the material anisotropy under different bi-axial stress states. In a multi-phase material, similar stress ratios imposed along different directions can result it different flow behaviour (Figure 17) as a result of the phase interactions. Direction dependent morphological features at the micro level, such as elongated grains from rolling, lath grains, matrix-fibre type arrangement etc., can significantly alter the shape of the yield locus unlike in our case with a homogeneous distribution of equiaxed grains. The approach can further be extended to the entire stress space to arrive at the full anisotropic yield locus of the multi-phase material.

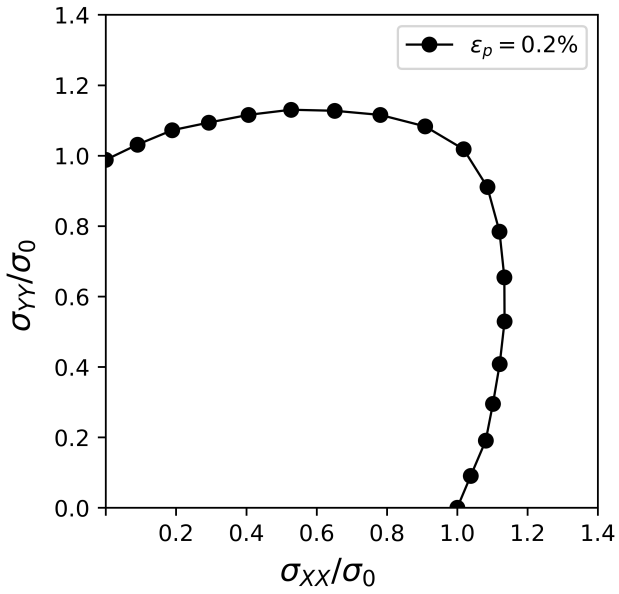

Figure 18: The normalized XX-YY yield section of Duplex steel RVE.

4.4. Other remarks

There have been several contributions in literature along the line of RVE based simulations of multi-phase materials, incorporating material anisotropy, employing different material laws and homogenization techniques, in conjuncture with different FE solvers. DAMASK [23] is one such promising open source multi-scale simulation framework. However, the RVE based simulations in DAMASK are performed either as direct CPFEM simulations or using the isostrain homogenization scheme (FC Taylor) with a single grain at every integration point. Also, computational efficiency is increased using a spectral solver, which has its own limitations such as the need for the microstructure to be representative (periodic in nature) and the boundary conditions to be periodic [64]. Also, the number of iterations for the solver, which is problem and grid specific, tends to influence the fulfilment of equilibrium causing the error to increase monotonically beyond the optimal limit. The optimal iterations are influenced by the contrast in local properties and hence, a very good

understanding of the underlying problem is essential to utilize such solvers. The multi-scale set up demonstrated by Srivastava et al. [2] focuses on RVE based methods for multi-phase materials, through rate-dependent phenomenological power law based CPFEM simulations. The RVE response is then used to calibrate macroscopic material definitions. The usage of CPFEM based RVE simulations of Dual Phase steels (DP) have gained momentum over the recent years as well [41, 65]. Such direct CPFEM simulations can be numerically expensive and coupling them with a macroscopic model in a multi-scale set up is virtually impossible. For example, in a study conducted by Dumoulin et al. [61] on different rate-dependent CPFEM algorithms, the total simulation time for a mesh containing $\sim$ 13000 elements was nearly 21 hours. The elements were cubic 8-node elements and the simulations were conducted on 8-equivalent CPUs. This, in comparison to our simulation time of 2 hour for a mesh containing 64000 elements in a Intel Xeon 2.8GHz processor without parallelization, is much higher. Thus, the aforementioned disadvantages are mitigated through our current approach based on plastic potential functions and the model can provide a somewhat elegant solution to couple a multi-phase 3D meso-scale representative microstructure to a macroscopic model. By defining plastic potential functions in the stress space, a yield locus expression is readily available and this can speed up the calculation time in elasto-plastic FEM. However, it has to be noted that the evolution of grain orientations has not yet been implemented in this model and hence it cannot predict texture changes.

The current model eventually supplements different options to couple the meso-scale RVE to macroscopic simulations: (1) The yield locus extracted from the multi-phase RVE can be used as inputs for the macroscopic model, (2) The macro- and meso-scale simulations can be coupled through a one-way approach (like submodelling in Abaqus) with the output from the former serving as the input for the latter, (3) The meso-scale simulations can be used to calibrate anisotropic yield functions or plastic potential functions which would then function as material laws for the macroscopic model, and (4) Direct FE^2 [66, 67] multi-scale simulations can also be performed.

5. Conclusion

A novel and efficient method to perform meso-scale simulations on the 3D microstructure of multi-phase steel was presented in this article. The homogenized response from the meso-scale would then characterize the macroscopic material behaviour. The model was evaluated by performing numerical simulations on a synthetic Duplex steel microstructure generated using parameters procured from literature. The simulated results were assessed with the experimental data from uniaxial tensile test and Neutron Diffraction studies of the same reference material. Finally, a method to construct the anisotropic yield section of the microstructure was demonstrated. The following are the important highlights from the study performed:

1. Single crystal plastic potential functions were derived via the Facet method. The increase in order of the function results in a yield locus which is in very good agreement with the theoretical one.
2. The flow curves predicted by the numerical model were in good correspondence with the experimental data. The small deviations at lower strains were primarily due to the fitted grain hardening laws. Hence, the choice of the grain hardening curve is crucial to get reasonable macroscopic predictions.
3. The numerical anisotropy calculations of the lattice strains along different diffraction planes, from the simulations were presented. The austenite diffraction curves were overestimated by the numerical model. For the ferritic phase, the (200) case showed an exact match while the (211) results were underestimated. These deviations are primarily due to the morphological differences in phase distribution of the reference and synthetic microstructure and the negation of texture evolution effects in the current model. Also, by increasing the number of grains contributing to the lattice strain calculations (i.e. using larger RVEs), the deviations in the predictions seemed to get reduced for some diffraction planes.

4. The construction of an yield section of the synthetic multi-phase microstructure was demonstrated within the current framework. The steps followed are easily adaptable and can serve as a valuable tool in understanding the influence of different microstructural features on the macroscopic material anisotropy.

The ability to predict texture shall be implemented in the future so that the model has the ability to predict orientation changes due to large rotations during crystal deformations. It is also required to study the developed model further with different multi-phase materials of varied morphology and strong texture components to better understand its capabilities and limitations.

6. Acknowledgements

The authors are thankful for the financial support provided by the project "Development, Monitoring and Prediction of Coupled Interactions in Material Durability Testing (DeMoPreCI-MDT)", a part of SIM-Flanders, Belgium.

7. Data availability

The raw and processed data required to reproduce these findings cannot be shared at this time due to technical or time limitations.

References

[1] M. G. D. Geers, V. G. Kouznetsova, W. A. M. Brekelmans, Multi-scale computational homogenization: Trends and challenges, Journal of Computational and Applied Mathematics 234 (7) (2010) 2175–2182. doi:10.1016/j.cam.2009.08.077.

[2] A. Srivastava, A. F. Bower, L. G. Hector Jr, J. E. Carsley, L. Zhang, F. Abu-Farha, A multiscale approach to modeling formability of dual-phase steels, Modelling and Simulation in Materials Science and Engineering 24 (2) (2016) 025011. doi:10.1088/0965-0393/24/2/025011.

[3] W. Tan, Y. C. Shin, Multi-scale modeling of solidification and microstructure development in laser keyhole welding process for austenitic stainless steel, Computational Materials Science 98 (2015) 446–458. doi:10.1016/j.commatsci.2014.10.063.

[4] D.-F. Li, B. J. Golden, N. P. ODowd, Multiscale modelling of mechanical response in a martensitic steel: A micromechanical and length-scale-dependent framework for precipitate hardening, Acta Materialia 80 (2014) 445–456. doi:10.1016/j.actamat.2014.08.012.

[5] I. Watanabe, D. Setoyama, N. Nagasako, N. Iwata, K. Nakanishi, Multiscale prediction of mechanical behavior of ferrite-pearlite steel with numerical material testing, International Journal for Numerical Methods in Engineering 89 (7) (2012) 829–845. doi:10.1002/nme.3264.

[6] V. Uthaisangsuk, U. Prahl, W. Bleck, Characterisation of formability behaviour of multiphase steels by micromechanical modelling, International Journal of Fracture 157 (1) (2009) 55. doi:10.1007/s10704-009-9329-4.

[7] A. Ramazani, K. Mukherjee, H. Quade, U. Prahl, W. Bleck, Correlation between 2d and 3d flow curve modelling of dp steels using a microstructure-based rve approach, Materials Science and Engineering: A 560 (2013) 129–139. doi:10.1016/j.msea.2012.09.046.

[8] J. Zhou, A. M. Gokhale, A. Gurumurthy, S. P. Bhat, Realistic microstructural rve-based simulations of stressstrain behavior of a dual-phase steel having high martensite volume fraction, Materials Science and Engineering: A 630 (2015) 107–115. doi:10.1016/j.msea.2015.02.017.

[9] R. Quey, P. Dawson, F. Barbe, Large-scale 3d random polycrystals for the finite element method: Generation, meshing and remeshing, Computer Methods in Applied Mechanics and Engineering 200 (17) (2011) 1729–1745. doi:10.1016/j.cma.2011.01.002.

[10] M. A. Groeber, M. A. Jackson, Dream.3d: A digital representation environment for the analysis of microstructure in 3d, Integrating Materials and Manufacturing Innovation 3 (1) (2014) 5. doi:10.1186/2193-9772-3-5.

[11] R. Quey, P. R. Dawson, F. Barbe, Large-scale 3d random polycrystals for the finite element method: Generation, meshing and remeshing, Computer Methods in Applied Mechanics and Engineering 200 (17) (2011) 1729–1745. doi:10.1016/j.cma.2011.01.002.

[12] D. M. Turner, S. R. Kalidindi, Statistical construction of 3-d microstructures from 2-d exemplars collected on oblique sections, Acta Materialia 102 (2016) 136–148. doi:10.1016/j.actamat.2015.09.011.

[13] C. C. Tasan, J. P. M. Hoefnagels, M. Diehl, D. Yan, F. Roters, D. Raabe, Strain localization and damage in dual phase steels investigated by coupled in-situ deformation experiments and crystal plasticity simulations, International Journal of Plasticity 63 (2014) 198–210. doi:10.1016/j.ijplas.2014.06.004.

[14] C. C. Tasan, M. Diehl, D. Yan, C. Zambaldi, P. Shanthraj, F. Roters, D. Raabe, Integrated experimentalsimulation analysis of stress and strain partitioning in multiphase alloys, Acta Materialia 81 (2014) 386–400. doi:10.1016/j.actamat.2014.07.071.

[15] S. Meille, E. J. Garboczi, Linear elastic properties of 2d and 3d models of porous materials made from elongated objects, Modelling and Simulation in Materials Science and Engineering 9 (5) (2001) 371. doi:10.1088/0965-0393/9/5/303.

[16] S. Sodjit, V. Uthaisangsuk, Microstructure based prediction of strain hardening behavior of dual phase steels, Materials & Design 41 (2012) 370–379. doi:10.1016/j.matdes.2012.05.010.

[17] I. Gutiérrez, R.-M. Rodriguez, Unified formulation to predict the tensile curves of steels with different microstructures, Trans Tech Publications 426 (2003) 4525–4530. doi:10.4028/www.scientific.net/MSF.426-432.4525.

[18] N. Vajragupta, V. Uthaisangsuk, B. Schmaling, S. Mnstermann, A. Hartmaier, W. Bleck, A micromechanical damage simulation of dual phase steels using xfem, Computational Materials Science 54 (2012) 271–279. doi:10.1016/j.commatsci.2011.10.035.

[19] F. Roters, P. Eisenlohr, L. Hantcherli, D. D. Tjahjanto, T. R. Bieler, D. Raabe, Overview of constitutive laws, kinematics, homogenization and multiscale methods in crystal plasticity finite-element modeling: Theory, experiments, applications, Acta Materialia 58 (4) (2010) 1152–1211. doi:10.1016/j.actamat.2009.10.058.

[20] G. I. Taylor, Plastic strain in metals, Plastic Strain in Metals (1938) 307–324.

[21] J. Gawad, A. Van Bael, P. Eyckens, G. Samaey, P. Van Houtte, D. Roose, Hierarchical multi-scale modeling of texture induced plastic anisotropy in sheet forming, Computational Materials Science 66 (2013) 65–83. doi:10.1016/j.commatsci.2012.05.056.

[22] P. Van Houtte, S. Li, M. Seefeldt, L. Delannay, Deformation texture prediction: from the taylor model to the advanced lamel model, International

Journal of Plasticity 21 (3) (2005) 589–624. doi:10.1016/j.ijplas.2004.04.011.

[23] F. Roters, P. Eisenlohr, C. Kords, D. D. Tjahjanto, M. Diehl, D. Raabe, Damask: the dsseldorf advanced material simulation kit for studying crystal plasticity using an fe based or a spectral numerical solver, Procedia IUTAM 3 (2012) 3–10. doi:10.1016/j.piutam.2012.03.001.

[24] S. R. Kalidindi, Data science and cyberinfrastructure: critical enablers for accelerated development of hierarchical materials, International Materials Reviews 60 (3) (2015) 150–168. doi:10.1179/1743280414Y.0000000043.

[25] J. R. Rice, Inelastic constitutive relations for solids: An internal-variable theory and its application to metal plasticity, Journal of the Mechanics and Physics of Solids 19 (6) (1971) 433–455. doi:10.1016/0022-5096(71)90010-X.

[26] D. Peirce, R. J. Asaro, A. Needleman, An analysis of nonuniform and localized deformation in ductile single crystals, Acta Metallurgica 30 (6) (1982) 1087–1119. doi:10.1016/0001-6160(82)90005-0.

[27] L. Anand, M. Kothari, A computational procedure for rate-independent crystal plasticity, Journal of the Mechanics and Physics of Solids 44 (4) (1996) 525–558. doi:10.1016/0022-5096(96)00001-4.

[28] J. W. Hutchinson, Bounds and self-consistent estimates for creep of polycrystalline materials, The Royal Society 348 (1652) (1976) 101–127. doi:10.1098/rspa.1976.0027.

[29] R. J. Asaro, A. Needleman, Overview no. 42 texture development and strain hardening in rate dependent polycrystals, Acta Metallurgica 33 (6) (1985) 923–953. doi:10.1016/0001-6160(85)90188-9.

[30] S. R. Kalidindi, C. A. Bronkhorst, L. Anand, Crystallographic texture evolution in bulk deformation processing of fcc metals, Journal of the

Mechanics and Physics of Solids 40 (3) (1992) 537–569. doi:10.1016/0022-5096(92)80003-9.

[31] C. C. Tasan, J. P. M. Hoefnagels, M. Diehl, D. Yan, F. Roters, D. Raabe, Strain localization and damage in dual phase steels investigated by coupled in-situ deformation experiments and crystal plasticity simulations, International Journal of Plasticity 63 (2014) 198–210. doi:10.1016/j.ijplas.2014.06.004.

[32] S. Dumoulin, O. Engler, O. S. Hopperstad, O. G. Lademo, Description of plastic anisotropy in aa6063-t6 using the crystal plasticity finite element method, Modelling and Simulation in Materials Science and Engineering 20 (5) (2012) 055008. doi:10.1088/0965-0393/20/5/055008.

[33] F. Maresca, V. G. Kouznetsova, M. G. D. Geers, On the role of interlath retained austenite in the deformation of lath martensite, Modelling and Simulation in Materials Science and Engineering 22 (4) (2014) 045011. doi:10.1088/0965-0393/22/4/045011.

[34] P. Van Houtte, S. K. Yerra, A. Van Bael, The facet method: A hierarchical multilevel modelling scheme for anisotropic convex plastic potentials, International Journal of Plasticity 25 (2) (2009) 332–360. doi:10.1016/j.ijplas.2008.02.001.

[35] P. Van Houtte, Application of plastic potentials to strain rate sensitive and insensitive anisotropic materials, International Journal of Plasticity 10 (7) (1994) 719–748. doi:10.1016/0749-6419(94)90043-4.

[36] M. Darrieulat, D. Piot, A method of generating analytical yield surfaces of crystalline materials, International Journal of Plasticity 12 (5) (1996) 575–610. doi:10.1016/S0749-6419(98)80001-6.

[37] W. Gambin, Crystal plasticity based on yield surfaces with rounded-off corners, Zeitschrift fr angewandte Mathematik und Mechanik 71 (4) (1991) T265–T268.

[38] A. R. Zamiri, F. Pourboghrat, A novel yield function for single crystals based on combined constraints optimization, International Journal of Plasticity 26 (5) (2010) 731–746. doi:10.1016/j.ijplas.2009.10.004.

[39] S. R. Kalidindi, S. E. Schoenfeld, On the prediction of yield surfaces by the crystal plasticity models for fcc polycrystals, Materials Science and Engineering: A 293 (1) (2000) 120–129. doi:10.1016/S0921-5093(00)01048-0.

[40] C. U. Jeong, W. Woo, J. Y. Choi, S.-H. Choi, Effect of kinematic stability of initial orientation on deformation heterogeneity and ductile failure in duplex stainless steel during uniaxial tension, Acta Materialia 67 (Supplement C) (2014) 21–31. doi:10.1016/j.actamat.2013.12.020.

[41] W. Woo, V. T. Em, E.-Y. Kim, S. H. Han, Y. S. Han, S.-H. Choi, Stress-strain relationship between ferrite and martensite in a dual-phase steel studied by in situ neutron diffraction and crystal plasticity theories, Acta Materialia 60 (20) (2012) 6972–6981. doi:10.1016/j.actamat.2012.08.054.

[42] A. Baczmaski, N. Hfaiedh, M. Franois, K. Wierzbanowski, Plastic incompatibility stresses and stored elastic energy in plastically deformed copper, Materials Science and Engineering: A 501 (1) (2009) 153–165. doi:10.1016/j.msea.2008.09.072.

[43] T.-S. Han, P. Dawson, Lattice strain partitioning in a two-phase alloy and its redistribution upon yielding, Materials Science and Engineering: A 405 (1) (2005) 18–33. doi:10.1016/j.msea.2005.05.095.

[44] R. Logé, H. Turkmen, M. Miller, R. Rogge, P. Dawson, Influence of modelling variables on the distribution of lattice strains in a deformed polycrystal, with reference to neutron diffraction experiments, Modelling and Simulation in Materials Science and Engineering 12 (4) (2004) 633. doi:10.1088/0965-0393/12/4/006.

[45] M. Miller, J.-S. Park, P. Dawson, T.-S. Han, Measuring and modeling distributions of stress state in deforming polycrystals, Acta Materialia 56 (15) (2008) 3927–3939. doi:10.1016/j.actamat.2008.04.062.

[46] F. Barlat, H. Aretz, J. W. Yoon, M. E. Karabin, J. C. Brem, R. E. Dick, Linear transfomation-based anisotropic yield functions, International Journal of Plasticity 21 (5) (2005) 1009–1039. doi:10.1016/j.ijplas.2004.06.004.

[47] D. Banabic, F. Barlat, O. Cazacu, T. Kuwabara, Advances in anisotropy and formability, International Journal of Material Forming 3 (3) (2010) 165–189. doi:10.1007/s12289-010-0992-9.

[48] J. F. W. Bishop, R. Hill, A theory of the plastic distortion of a polycrystalline aggregate under combined stresses, The London, Edinburgh, and Dublin Philosophical Magazine and Journal of Science 42 (327) (1951) 414–427. doi:10.1080/14786445108561065.

[49] M. L. Wilkins, Calculation of elastic-plastic flow, Tech. rep., California Univ Livermore Radiation Lab (1963).

[50] O. van der Sluis, P. J. G. Schreurs, W. A. M. Brekelmans, H. E. H. Meijer, Overall behaviour of heterogeneous elastoviscoplastic materials: effect of microstructural modelling, Mechanics of Materials 32 (8) (2000) 449–462. doi:10.1016/S0167-6636(00)00019-3.

[51] S. Li, Boundary conditions for unit cells from periodic microstructures and their implications, Composites Science and Technology 68 (9) (2008) 1962–1974. doi:10.1016/j.compscitech.2007.03.035.

[52] S. Li, A. Wongsto, Unit cells for micromechanical analyses of particle-reinforced composites, Mechanics of Materials 36 (7) (2004) 543–572. doi:10.1016/S0167-6636(03)00062-0.

[53] P. Van Houtte, K. Mols, A. Van Bael, E. Aernoudt, Application of yield loci calculated from texture data, Textures and Microstructures 11 (1) (1989) 23–39. doi:10.1155/TSM.11.23.

[54] E. Aernoudt, J. Gil-Sevillano, P. Van Houtte, Structural background of yield and flow, Constitutive relations and their physical basis (S. I. Andersen, ed.) (1987) 1–38.

[55] H. Ghassemi-Armaki, P. Chen, S. Bhat, S. Sadagopan, S. Kumar, A. Bower, Microscale-calibrated modeling of the deformation response of low-carbon martensite, Acta Materialia 61 (10) (2013) 3640–3652. doi:10.1016/j.actamat.2013.02.051.

[56] E.-Y. Guo, H.-X. Xie, S. S. Singh, A. Kirubanandham, T. Jing, N. Chawla, Mechanical characterization of microconstituents in a cast duplex stainless steel by micropillar compression, Materials Science and Engineering: A 598 (2014) 98–105. doi:10.1016/j.msea.2014.01.002.

[57] T. T. Huang, R. B. Gou, W. J. Dan, W. G. Zhang, Strain-hardening behaviors of dual phase steels with microstructure features, Materials Science and Engineering: A 672 (2016) 88–97. doi:10.1016/j.msea.2016.06.066.

[58] N. Jia, R. Lin Peng, Y. D. Wang, S. Johansson, P. K. Liaw, Micromechanical behavior and texture evolution of duplex stainless steel studied by neutron diffraction and self-consistent modeling, Acta Materialia 56 (4) (2008) 782–793. doi:10.1016/j.actamat.2007.10.040.

[59] N. Jia, R. Lin Peng, D. Brown, B. Clausen, Y. Wang, Tensile deformation behavior of duplex stainless steel studied by in-situ time-of-flight neutron diffraction, Metallurgical and Materials Transactions A 39 (13) (2008) 3134. doi:10.1007/s11661-008-9675-2.

[60] J. C. Tucker, A. R. Cerrone III, A. R. Ingraffea, A. D. Rollett, Crystal plasticity finite element analysis for rené88dt statistical volume element

generation, Modelling and Simulation in Materials Science and Engineering 23 (3) (2015) 035003. doi:10.1088/0965-0393/23/3/035003.

[61] S. Dumoulin, O. S. Hopperstad, T. Berstad, Investigation of integration algorithms for rate-dependent crystal plasticity using explicit finite element codes, Computational Materials Science 46 (4) (2009) 785–799. doi:10.1016/j.commatsci.2009.04.015.

[62] F. J. Harewood, P. E. McHugh, Comparison of the implicit and explicit finite element methods using crystal plasticity, Computational Materials Science 39 (2) (2007) 481–494. doi:10.1016/j.commatsci.2006.08.002.

[63] E. Gürses, M. Becker, C. Miehe, Numerical computation of anisotropically evolving yield surfaces based on micro-to-macro transitions, PAMM 4 (1) (2004) 219–220. doi:10.1002/pamm.200410091.

[64] R. A. Lebensohn, N-site modeling of a 3d viscoplastic polycrystal using fast fourier transform, Acta Materialia 49 (14) (2001) 2723–2737. doi:10.1016/S1359-6454(01)00172-0.

[65] J. Kadkhodapour, A. Butz, S. Ziaei-Rad, S. Schmauder, A micro mechanical study on failure initiation of dual phase steels under tension using single crystal plasticity model, International Journal of Plasticity 27 (7) (2011) 1103–1125. doi:10.1016/j.ijplas.2010.12.001.

[66] P. Raghavan, S. Ghosh, Concurrent multi-scale analysis of elastic composites by a multi-level computational model, Computer Methods in Applied Mechanics and Engineering 193 (6) (2004) 497–538. doi:10.1016/j.cma.2003.10.007.

[67] C. Hirschberger, S. Ricker, P. Steinmann, N. Sukumar, Computational multiscale modelling of heterogeneous material layers, Engineering Fracture MechanicsEngineering Fracture Mechanics 76 (6) (2009) 793–812. doi:10.1016/j.engfracmech.2008.10.018.